Peierls-type structural phase transition in the low-dimensional superconductor Sc$_3$CoC$_4$

Jan Langmann ●, Marcel Vöst, Andreas Fischer ●, Hasan Kepenci ●, Georg Eickerling ●,[*] and Wolfgang Scherer
CPM, Institut für Physik, Universität Augsburg, 86159 Augsburg, Germany

Luigi Paolasini ● and Alexei Bosak
European Synchrotron Radiation Facility, BP 220, 38043 Grenoble Cedex, France

Leila Noohinejad and Martin Tolkiehn
P24, PETRA III, Deutsches Elektronen-Synchrotron DESY, Notkestraße 85, 22607 Hamburg, Germany

We provide information about the progression of the structurally low-dimensional superconductor Sc$_3$CoC$_4$ from its high-temperature phase to its Peierls-type distorted low-temperature phase. Results from inelastic x-ray scattering, diffuse scattering, and high-resolution x-ray diffraction experiments provide conclusive evidence that the onset of a modulation in the atomic positions during the structural transition is primarily driven by a combination of phonon softening and order-disorder transition. The completion of the phonon softening process at ∼150 K is found to be followed by two additional stages, i.e., an accumulation of gradual structural changes between 150 and 80 K and their saturation into the final low-temperature phase structure below ∼80 K.

I. INTRODUCTION

Per definition the onset of superconductivity affects the electron system of a material by coupling electrons into Cooper pairs [1]. However, the emergence of superconductivity critically depends on a suitable phononic and electronic structure and consequently on the electronic nature of the atoms in the host lattice and their chemical connectivity. This reasoning is driving an ever increasing number of *ab initio* efforts to discover new superconductors [2,3] and has led to the successful prediction of superconductivity in H$_3$S [4,5] and LaH$_{10}$ [6,7] under high pressure and at record-high temperatures.

However, the arrangement of atoms in the crystal structure of a superconductor does not necessarily remain stable upon cooling from room temperature towards its T_c. At present, a wide and diverse field of compounds is known, where small structural changes occur that either are in competition with the onset of superconductivity, leave it unaffected, or even lead to its stabilization [8–26]. These structural changes can be subtle and solely indicated by an anomaly in the thermal expansion directly above the T_c as exemplified by the broadly known MgB$_2$ [27–29]. However, they may also break the rotational and/or translational symmetry of the crystal structure as demonstrated by the trigonal-to-triclinic phase transitions in the Chevrel phases [8–10,26,30–32] or the tetragonal-to-orthorhombic phase transitions in the iron-based superconductors [12–16,33]. Intriguing hybrids between electronic and structural phase transitions are the charge-density waves forming in quasi-one-dimensional [34–37] and quasi-two-dimensional (quasi-2D) superconductors [35,38–44] as well as copper-oxide-based superconductors [17–25,35].

Also in the transition-metal carbide Sc$_3$CoC$_4$ [45–57], a Peierls-type structural phase transition from an orthorhombic high-temperature (HT) phase (space group *Immm*, No. 71 [58]) to a monoclinic low-temperature (LT) phase (space group $C2/m$, No. 12 [58]) is potentially related to the formation of its superconducting phase. The crystal structure of the compound (Fig. 1) is coined by a low-dimensional motif featuring infinite [Co(C$_2$)$_2$]$_\infty$ ribbons (joined by sticks in Fig. 1). In the undistorted high-temperature phase, these ribbons are aligned along the crystallographic b_{HT} axis and form quasi-2D layers in the a_{HT}-b_{HT} plane by an alternating stacking with scandium atoms (labeled as Sc1; pink spheres in Fig. 1). These layers are in turn structurally separated by interjacent layers of scandium atoms (labeled as Sc2; orange spheres in Fig. 1).

Upon cooling to temperatures below 80 K, the Peierls-type structural distortion in Sc$_3$CoC$_4$ leads to a modulation of the positions of Co and Sc1 atoms within the a_{HT}-b_{HT} plane, before superconductivity sets in at $T_c \approx 4.5$ K [46–50,54,56]. Application of pressure simultaneously raises the onset temperature of the structural distortion and drastically increases the superconducting sample fraction while leaving the superconducting T_c unchanged [51,57]. Recently, we provided experimental and theoretical evidence hinting at the existence of a soft phonon mode causing dynamic LT-phase-like structural distortions already at room temperature [50]. It is also this phonon mode that seems to be a key driver of the superconductivity in Sc$_3$CoC$_4$, as pointed out by theoretical work of Zhang *et al.* [55].

In the following, we present experimental results from temperature-dependent x-ray diffraction and inelastic x-ray
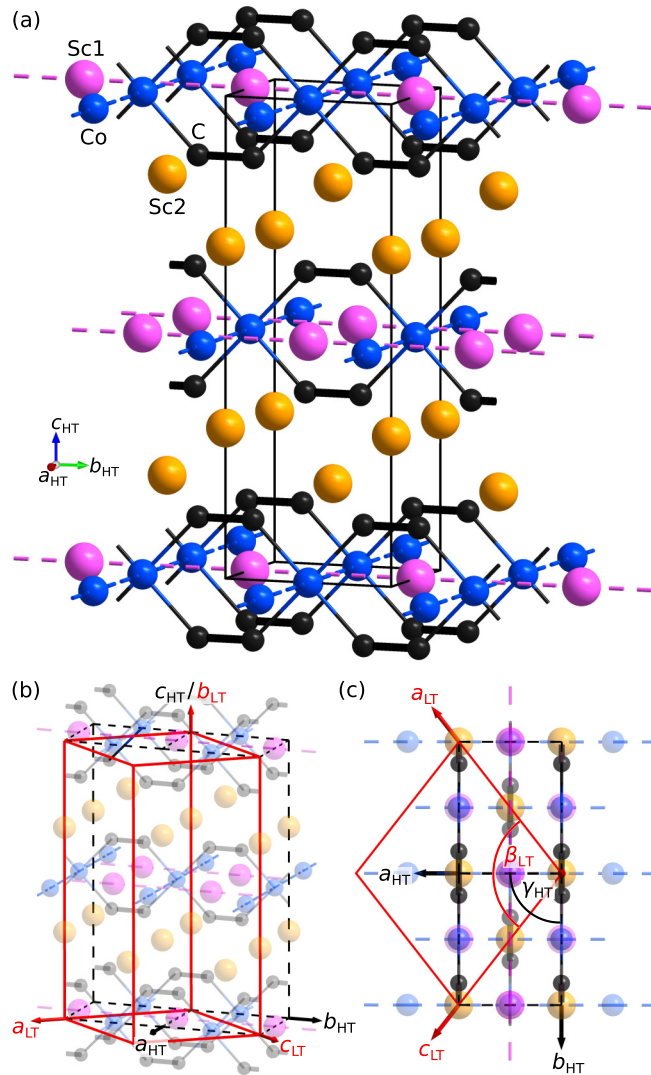
*georg.eickerling@uni-a.de

FIG. 1. (a) Ball-and-stick representation of the structure of Sc_3CoC_4 in its orthorhombic high-temperature (HT) phase. Infinite $[Co(C_2)_2]_\infty$ ribbons are aligned along the b_{HT} axis and connected into layers in the a_{HT}-b_{HT} plane by interjacent scandium atoms (labeled as Sc1). Additional linear chains of Co and Sc1 atoms within the layers (indicated by dashed lines) span along the a_{HT} and b_{HT} axes, respectively. Neighboring Co-Sc1-C layers along the c_{HT} axis are structurally separated from each other by layers composed exclusively from scandium atoms (labeled as Sc2). In (b) and (c) the cell transformation relating the unit cells of the orthorhombic HT-phase structural model (dashed black lines) and the monoclinic LT-phase structural model in its conventional setting [45–52] (solid red lines) is visualized in views towards the b_{HT}-c_{HT} plane (b) and the a_{HT}-b_{HT} plane (c).

scattering studies which provide more detailed insight into the progression of Sc_3CoC_4 towards its structural distortion.

II. METHODS

A. Investigated samples

Needle-shaped single crystals of Sc_3CoC_4 were grown according to methods described elsewhere [45,46,51,56]. Single crystals investigated in inelastic x-ray scattering (IXS), diffuse scattering (DS), and x-ray diffraction (XRD) experiments under ambient-pressure conditions had typical dimensions of approximately $50 \times 50 \times 200$ µm^3 (full experimental details can be found in the Supplemental Material [59]).

B. Inelastic x-ray scattering

The IXS experiments were conducted using the high-resolution spectrometer at beamline ID28 of the European Synchrotron Radiation Facility (ESRF; see Refs. [60,61] for a description of the beamline layout). Energy scans with a resolution of 3 meV (full width at half maximum) were taken at positions (2,0,0) and $(3, \bar{1}, 0)$ employing an incident beam with energy 17.8 keV ($\lambda = 0.6968$ Å) monochromatized by a silicon backscattering monochromator set at the (9,9,9) reflection order. Phonon energies were extracted from the collected IXS spectra by least-squares fitting with a damped harmonic oscillator model as implemented in the software FIT28 [62]. Calculated IXS spectra were thereby folded with an instrumental energy resolution function as determined in the measurement of the elastic line of an acrylic glass [poly(methyl methacrylate) (PMMA)] sample at a temperature of 15 K.

C. Diffuse x-ray scattering

Measurements of the DS and temperature-dependent variations in the Bragg peak positions were carried out at the side station of beamline ID28 at the ESRF using a monochromatic beam with the same energy as in the IXS experiments (17.8 keV) and the energy-integrating hybrid-pixel detector Dectris PILATUS3 X 1M. Diffuse scattering features were studied by means of reconstructed sections of reciprocal space generated with the program CRYSALISPRO [63]. Peak position analyses were performed by means of a program locally developed at beamline ID28 using orientation matrices and instrument models from the program CRYSALISPRO [63] as input. The experimental setups for the investigation of IXS, DS, and reflection positions relied on Oxford open-flow N$_2$ coolers [64] to reach low temperatures in the range between 80 and 300 K.

D. X-ray diffraction

Single-crystal XRD data under ambient-pressure conditions were collected employing three different experimental setups: Synchrotron XRD experiments were performed at beamline P24 of the PETRA III extension at the Deutsches Elektronen-Synchrotron (DESY) using a monochromatic beam with energy 24.8 keV ($\lambda = 0.5000$ Å), a Huber four-circle Eulerian cradle goniometer, and the hybrid-pixel detector Dectris PILATUS3 X CdTe 1M. Sample temperatures in the range between 50 and 175 K were thereby realized by means of a Cryocool open-flow cooler employing helium as a cooling gas. Resulting XRD data were processed with the program CRYSALISPRO [65] to generate reconstructed sections of reciprocal space with high resolution.

Laboratory-scale XRD experiments in the temperature range between 80 and 300 K were performed using a Bruker SMART APEX diffractometer featuring a D8 goniometer,

an Incoatec AgK$_\alpha$ microfocus sealed-tube x-ray source ($\lambda =$ 0.560 87 Å), an APEX II charge-coupled device (CCD) detector, and an Oxford open-flow N$_2$ cooler [64] (subsequently referred to as "laboratory-scale instrumental setup 1"). The collected XRD data sets were processed using the program SAINT [66] to determine unit cell parameters and reflection intensities corresponding to the orthorhombic and monoclinic unit cells of HT-phase and LT-phase structural models.

Additional laboratory-scale XRD experiments in the temperature range between 10 and 300 K were performed employing a Huber four-circle Eulerian cradle goniometer fitted with an Incoatec AgK$_\alpha$ microfocus sealed-tube x-ray source ($\lambda = 0.560\,87$ Å), a Dectris PILATUS3 R CdTe 300K hybrid-pixel detector, and an Advanced Research Systems closed-cycle helium cryocooler with domed beryllium vacuum and radiation shields (subsequently referred to as "laboratory-scale instrumental setup 2"; see Ref. [52] for a detailed description). The collected XRD data sets were processed using the program EVAL14 [67–69] to determine unit cell parameters and reflection intensities corresponding to the orthorhombic and monoclinic unit cells of HT-phase and LT-phase structural models.

Reflection intensities obtained from both laboratory-scale instrumental setups were subjected to scaling and absorption correction using the programs SADABS [70,71] (HT-phase structural models) or TWINABS [71,72] (LT-phase structural models). On this basis, least-squares structural refinements at the independent-atom-model (IAM) level were performed with the program JANA2006 [73,74].

E. Density functional theory calculations

Electronic structure calculations based on density functional theory (DFT) have been performed employing the WIEN2K package [75,76]. Starting points of the electronic structure calculations on Sc$_3$CoC$_4$ at room temperature (RT), 100 K, and 12 K were the XRD structural models in this paper. Reciprocal-space sampling for the self-consistent field cycles employing the Perdew-Burke-Ernzerhof (PBE) density functional [77,78] and the density of states calculations was done on a $21 \times 21 \times 21$ mesh of 1331 irreducible k points for the orthorhombic HT phase and a $22 \times 20 \times 22$ mesh of 2530 irreducible k points for the monoclinic LT phase. The muffin-tin radii were set to 2.20, 2.40, and 1.37 bohrs for cobalt, scandium, and carbon atoms, respectively, and $R_{mt}K_{max} = 8.0$ and $l_{max} = 10$ were used throughout. For the graphical representation of the total and site-projected density of states a Gaussian broadening of 0.001 was applied. Phonon dispersion relations have been obtained based on the calculations published earlier in Ref. [51]. To avoid an unnecessary backfolding of the phonon branches, the dispersion relations have been calculated with respect to the primitive unit cell.

III. THE PEIERLS-TYPE STRUCTURAL DISTORTION IN Sc$_3$CoC$_4$

The presence of a Peierls-type structurally distorted low-temperature phase in the transition-metal carbide Sc$_3$CoC$_4$ has been observed in several earlier investigations [46–52]. It could be shown that the structural changes between the
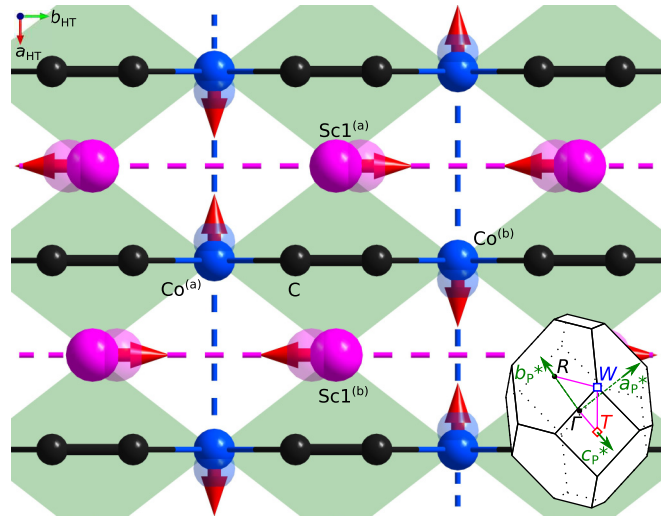

FIG. 2. Sketch of the basic atomic displacement pattern in the a_{HT}-b_{HT} plane that characterizes the phonons in the soft branch between high-symmetry points T and W of the phonon dispersion of HT-Sc$_3$CoC$_4$. Note that linear chains of Co and Sc1 atoms are indicated by dashed lines and that Sc2 atoms have been omitted for clarity. The Brillouin zone corresponding to the orthorhombic unit cell of the HT-phase structural model is sketched as an inset at the bottom right with primitive reciprocal cell axes indicated by green arrows.

high-temperature (HT) phase (space group $Immm$, No. 71 [58]) and the low-temperature (LT) phase of the compound (space group $C2/m$, No. 12 [58]) mainly affect linear chains of Co and Sc1 atoms spanning along the a_{HT} axis and the b_{HT} axis, respectively (highlighted by dashed lines in Figs. 1 and 2). While the atoms within the chains are equispaced in the HT phase, they form Co-Co and Sc1-Sc1 dimers in the LT phase. This basic distortion pattern was also found to persist in subtly modified form under hydrostatic pressure [51,52].

The reduction of the space group symmetry due to the Peierls-type structural distortion proceeds via two steps, i.e., a *translationengleiche* ($t2$) step from space group $Immm$ to space group $I112/m$ followed by an *isomorphe* ($i2$) step to space group $B112/m$ (unconventional setting). Subsequent standardization of the unit cell setting leads to space group $C2/m$ in line with literature records [46,48,49]. A Bärnighausen diagram of the symmetry thinning can be found in Fig. S1 of the Supplemental Material [59].

Taking into account the aforementioned symmetry characteristics, the HT-LT phase transition in Sc$_3$CoC$_4$ can be classified as improper ferroelastic [79–81]. Consequently, it may be accompanied by the formation of antiphase domains as well as (pseudo)merohedral twin domains with two distinct orientation states [79,82,83] related, for example, by a mirror plane perpendicular to the a_{HT} axis. The presence of twinning in LT-Sc$_3$CoC$_4$ is clearly recognized in XRD data collected at ambient pressure [46–52], although definitive experimental information about the explicit spatial arrangement of twin domains in the crystal is still lacking. Application of pressure has been observed to favor one twin domain state over the other leading to a detwinning of the sample [51,52].

Although a continuous second-order transition from the HT-phase space group $Immm$ to the LT-phase space group

$C2/m$ is allowed by symmetry arguments [84], the HT-LT transition in Sc_3CoC_4 at ambient pressure seems to proceed from the HT phase [stage (i)] via an intermediate stage between 149 and 82 K [stage (ii)] to the final LT phase below 82 K [stage (iii)]. However, the assertion of an intermediate stage of the HT-LT transition in Sc_3CoC_4 has been entirely phenomenological. It is based on the observation that the superstructure reflections characteristic of the reduction of translational symmetry in the monoclinic LT phase already appear at 149 K and not just below 82 K. In particular, cooling to below 149 K first leads to a *gradual* increase of the intensity at the superstructure reflection positions and then to another *jumplike* intensity increase at 82 K [see the red and green diamonds in Fig. 3(b)], while there is no experimental evidence for any further global symmetry reduction at this temperature [50,51]. Furthermore, distinct anomalies are observed in the electrical resistivity and the magnetization of Sc_3CoC_4 samples at both 149 and 82 K [47–51,57].

A previous combined diffuse x-ray scattering and density functional theory (DFT) study [50] suggested that the instability of Sc_3CoC_4 towards a Peierls-type structural distortion might be related to a soft branch between high-symmetry points W and T of the phonon dispersion relation of HT-Sc_3CoC_4 (a sketch of the Brillouin zone is given as an inset in Fig. 2). All soft phonons along the path W–T involve rotations of $Co^{(a)}$-$Sc1^{(a)}$-$Co^{(b)}$-$Sc1^{(b)}$ quadrangles in the a_{HT}-b_{HT} plane about the c_{HT} axis with opposing rotation senses for adjacent quadrangles along the b_{HT} axis (Fig. 2; $Co^{(a)}$-$Sc1^{(a)}$-$Co^{(b)}$-$Sc1^{(b)}$ quadrangles indicated in green). This translates into dynamic displacements of the Co atoms along $\pm a_{HT}$ and the Sc1 atoms along $\pm b_{HT}$, so that long and short distances form in the Co and Sc1 atom chains (dashed lines in Fig. 2) consistent with the reported static displacements in the Peierls-type distorted LT-phase structure [46–52].

Progression along the path from T to W adds varying degrees of modulation to the Co and Sc1 atomic displacements within the a_{HT}-b_{HT} plane along the c_{HT} axis. While no additional modulation is present at T (irreducible representation T_1^+), modulations with decreasing wavelengths arise between T and W (irreducible representation P_1), so that atomic displacements in next-nearest-neighbor layers along c_{HT} are finally inverted at W (irreducible representation W_2). Thereby, only atomic displacements according to the irreducible representation T_1^+ correspond to the reported LT-phase space group $C2/m$ [46–52,80].

So far, however, experimental evidence correlating the proposed phonon softening mechanism with the observed three phenomenological stages of the Peierls-type structural distortion in Sc_3CoC_4 is missing. In the following, we will first focus on an in-depth study of stage (i) ($T \gtrsim 150$ K) during the HT-LT transition of Sc_3CoC_4 by referring to diffuse x-ray scattering and inelastic x-ray scattering techniques.

IV. RESULTS

A. Diffuse x-ray scattering

Previous reports suggesting the existence of a soft branch in the phonon dispersion of the high-temperature (HT)
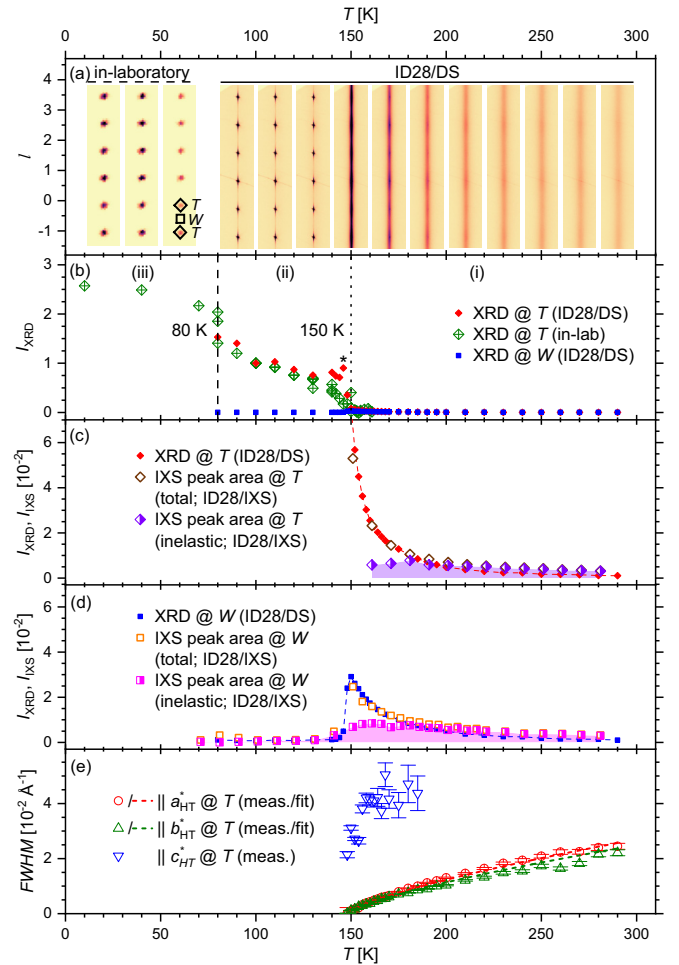

FIG. 3. (a) Temperature-dependent development of the diffuse rods spanning between reciprocal-space positions corresponding to the high-symmetry points T and W in the Brillouin zone for the orthorhombic HT-phase structure of Sc_3CoC_4. Scattered intensities I_{XRD} integrated over boxes of 30×30 pixels around positions $(3.5, 0.5, 0)$ ($\hat{=} T$) and $(3.5, 0.5, 0.5)$ ($\hat{=} W$) are given in (b) and on enlarged intensity scales in (c) and (d) [85]. Additionally, the total and inelastically scattered (phonon) intensities I_{IXS} as determined from IXS measurements are indicated by empty brown and half-filled purple symbols in (c) and by empty orange and half-filled magenta symbols in (d), respectively. The FWHM of the diffuse scattering above 150 K along reciprocal-space axes a_{HT}^*, b_{HT}^*, and c_{HT}^* is plotted in (e). Dashed lines represent power-law fits [FWHM $\sim ((T - T_P)/T_P)^\nu$] with $\nu = 0.73$. We note that the results are compiled from IXS data measured (meas.) at the high-resolution spectrometer of beamline ID28 (ID28/IXS) as well as in-laboratory XRD experiments from Ref. [50] and XRD data measured at the diffuse scattering side station of beamline ID28 (ID28/DS). Furthermore, a temperature shift of -9 K has been applied to the IXS data [86].

phase of Sc_3CoC_4 hinged on the observation of prominent diffuse x-ray scattering for relatively large and irregular-shaped single-crystalline samples and an in-laboratory x-ray source [50]. In these studies, diffuse rods spanning between reciprocal-space positions $(h + 0.5, k + 0.5, l)$ and $(h + 0.5, k + 0.5, l + 0.5)$, with h, k, and l having integer values, were observed. In order to exclude parasitic scatter-

ing due to crystal defects such as static disorder as the sole origin of these scattered intensities, we have as a first step of our present study repeated the diffuse x-ray scattering experiments employing small single-crystalline needles of high quality and synchrotron radiation.

Figure 3 summarizes the results of these diffuse scattering experiments on Sc_3CoC_4. The expected diffuse rods are clearly visible in reconstructed reciprocal-space planes $(h\,0.5\,l)$ already at 290 K (Fig. 3(a); see also Figs. S3–S6 in the Supplemental Material [59]). Provided that the diffuse scattering is of lattice-dynamical origin, the intensities at positions along a rod may indeed be linked to the frequencies along the soft branch in the phonon dispersion of HT-Sc_3CoC_4 [50]. Namely, large diffuse scattering intensity at positions $(h + 0.5, k + 0.5, l)$ [diamond symbols in Figs. 3(b) and 3(c)] and $(h + 0.5, k + 0.5, l + 0.5)$ [square symbols in Figs. 3(b) and 3(d)] relates to low phonon frequencies at the high-symmetry points T and W in the Brillouin zone (inset in Fig. 2), respectively.

The existence of a phonon softening mechanism in Sc_3CoC_4 should now translate into a temperature-dependent variation of the phonon frequencies in the soft $W–T$ branch and therefore of the intensity distribution along the diffuse rods. Indeed, lowering the sample temperature from 290 K leads to an initial simultaneous increase of the diffuse intensities I_{XRD} at all points along the diffuse rods. This can be recognized from the reconstructed reciprocal-space planes in Fig. 3(a) as well as the enlarged plots of the temperature dependence of $I_{XRD}(T)$ in Figs. 3(c) and 3(d). Below ∼180 K, I_{XRD} grows stronger at T than at W, so that the diffuse rods gradually contract into pinpoint superstructure reflections at T. At ∼150 K, i.e., the lower end of the temperature regime of stage (i) of the HT-LT transition in Sc_3CoC_4 defined in Sec. III, the diffuse intensity at T strongly increases, while it drops sharply to nearly zero at W [87] (Figs. 3(c) and 3(d); profile cuts of the scattered intensity can be found in Figs. S7–S13 of the Supplemental Material [59]). In line with earlier observations [50,51], this marks the onset of clearly recognizable superstructure reflections and thus the transition into the intermediate stage [stage (ii)] of the HT-LT transition of Sc_3CoC_4 (see Sec. III). Further cooling from 150 K down to 80 K is accompanied by a gradual increase of the superstructure reflection intensity $I_{XRD}(T)$ [85]. The realization of the final stage [stage (iii)] of the HT-LT transition characterized by an additional upward jump in $I_{XRD}(T)$ and its subsequent saturation in our previous in-laboratory studies could not be investigated in the new diffuse scattering experiments due to limitations of the employed low-temperature setup (see Sec. II). For reference, reciprocal-space reconstructions below 80 K and intensity data points from Ref. [50] have been added to Figs. 3(a) and 3(b).

A complementary view of the gradual emergence of the Peierls-type distorted structure during stage (i) of the HT-LT transition of Sc_3CoC_4 is provided by the temperature-dependent decrease of the full widths at half maximum (FWHM) of the diffuse scattering along reciprocal cell axes a_{HT}^*, b_{HT}^*, and c_{HT}^* upon cooling [Fig. 3(e)]. This is due to the fact that a *decrease* of the FWHM of the diffuse scattering relates to an *increase* of the inverse correlation lengths of pretransitional structural fluctuations along real-space cell axes a_{HT}, b_{HT}, and c_{HT}. In Fig. 3(e), the temperature dependence of the FWHM from Lorentzian fits of the diffuse scattering data at T is displayed. Nearly identical FWHM values along a_{HT}^* and b_{HT}^* (corresponding to the inverse correlation lengths along directions a_{HT} and b_{HT} within the plane of the Co-Sc1-C layers) at all investigated temperatures and drastically increased FWHM values along c_{HT}^* (corresponding to the layer stacking direction c_{HT}) emphasize the proposed quasi-2D character of Sc_3CoC_4 [50,51]. Above 185 K, the FWHM along c_{HT}^* can no longer reliably be determined, as the intensity of the diffuse rods is nearly homogeneous along this reciprocal-space axis. The FWHM along the other reciprocal-space axes, a_{HT}^* and b_{HT}^*, is found to follow power laws of the type $A \cdot ((T - T_P)/T_P)^v$ with $T_P = 148$ K, $v = 0.73$, and different prefactors A [dashed lines in Fig. 3(e)].

B. Inelastic x-ray scattering

Up to this point, the attribution of the diffuse scattering features of Sc_3CoC_4 above 150 K to a lattice-dynamical origin hinges on a visual comparison with *ab initio* thermal diffuse scattering (TDS) simulations and the general compatibility of the location and orientation of the diffuse rods in reciprocal space [50]. To provide more concrete evidence for this hypothesis, we performed inelastic x-ray scattering (IXS) measurements at reciprocal-space positions corresponding to the path between W and T which allow us to differentiate between elastically and inelastically scattered intensity. Integration of the total IXS spectra [Figs. 4(a) and 4(b)] and their inelastic portions with respect to energy leads to the temperature dependencies denoted by open brown and half-filled purple symbols in Fig. 3(c) and by open orange and half-filled magenta symbols in Fig. 3(d). After scaling and applying a temperature shift of −9 K [86], the total IXS intensity closely follows the temperature dependence of the total diffusely scattered intensity [filled red and blue symbols in Figs. 3(c) and 3(d)]. Furthermore, it becomes evident that the detected intensity I_{XRD} at T and W above ∼220 K is of purely inelastic nature. The underlying soft branch can be readily identified in the phonon dispersion of HT-Sc_3CoC_4 along the high-symmetry path $R–W–T–\Gamma$ (Fig. 5) [88].

Reducing the sample temperature towards 160 K entails a notable downward energy shift of the whole $W–T$ phonon branch (Fig. 5). A more complete impression of the lattice-dynamical changes can be gained from Fig. 4: The IXS spectra depicted in Figs. 4(a) and 4(b) point out that with decreasing temperature the centers of the phonon peaks (highlighted by black circles) at T and W gradually move to lower energies (an extensive overview of collected IXS spectra can be found in Figs. S14–S19 of the Supplemental Material [59]).

Temperature dependencies of the squared phonon energies as obtained from damped harmonic-oscillator fits are compiled in Fig. 4(c): Upon cooling towards 160 K, the squared phonon energies between T and W reduce linearly with nearly identical slopes and retain an overall flat course of the whole $W–T$ phonon branch. However, whereas the phonon at T (corresponding to the location of the superstructure reflections) reaches approximately zero energy at 160 K, the phonons at W and midway between T and W attain small, but finite energies. Cooling to even lower temperatures leads to a
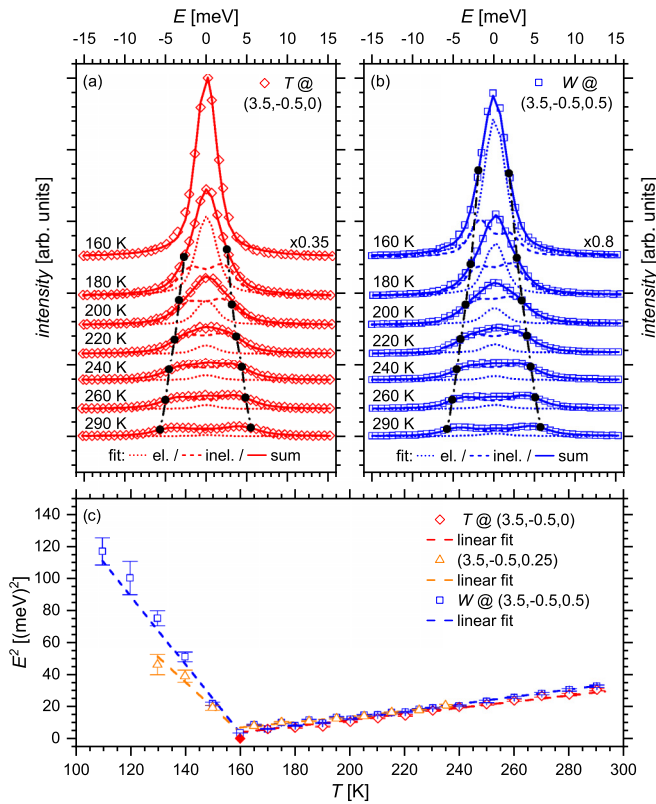
FIG. 4. Temperature-dependent development of IXS spectra between 290 and 160 K taken at reciprocal-space positions corresponding to the high-symmetry points (a) T and (b) W in the Brillouin zone of the HT phase of Sc_3CoC_4. Dotted, dashed, and solid lines represent fits to the elastic (el.) central peaks, the inelastic (inel.) excitation peaks (center marked by black circles), and their sums, respectively. The resulting temperature dependencies of the squared phonon energies at T and W and at an additional point in between are plotted in (c). Note that the spectrum corresponding to T at 160 K (a) could only be successfully described in a least-squares fit involving a single elastic central peak and that in (c) a tentative data point at 0 meV^2 (filled diamond symbol) has been added.
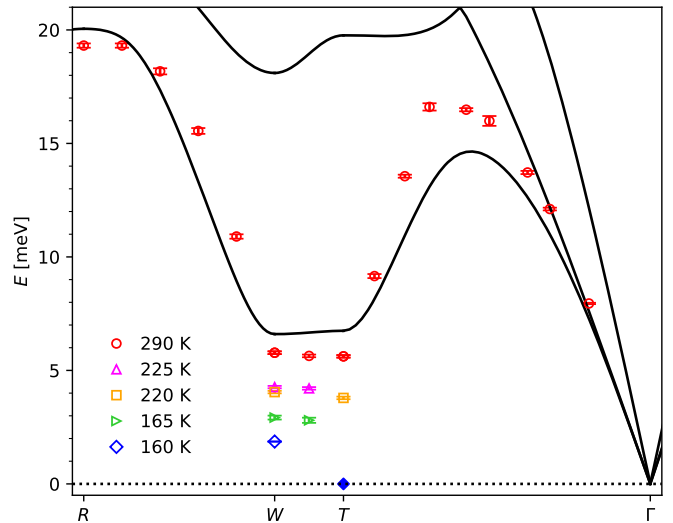

FIG. 5. Overlay of measured phonon mode energies at temperatures between 290 and 160 K (symbols) and a phonon dispersion relation for HT-Sc_3CoC_4 obtained from DFT calculations (energies scaled by a factor of 0.88; black lines). Note that a tentative data point at 0 meV corresponding to the high-symmetry point T at 160 K has been added (filled diamond symbol) as a guide to the eye (see also the caption of Fig. 4).

reincrease of the phonon energies at the latter two positions with much larger slopes than in the preceding regime of decreasing phonon energies above 160 K [ratios of the slopes between 9.3 and 9.5; Fig. 4(c)]. Such an emergence of significant energy differences along the previously flat W–T phonon branch might relate to an increased coupling between the atomic displacements within adjacent quasi-2D layers of Sc_3CoC_4. The phonon modes between high-symmetry points W and T all feature the same basic LT-phase-like atomic displacement pattern within the quasi-2D layers of Sc_3CoC_4 (visualized in Fig. 2) and only differ in the wavelength of an additional modulation of the atomic displacements along the stacking direction c_{HT}. Consequently, an increasing slope of the W–T phonon branch correlates with an increasing energy cost of introducing layer-wise modulations into the LT-phase-like atomic displacements in Fig. 2.

Irrespective of its ongoing softening towards 150 K, the W–T phonon branch only makes up a nearly temperature-independent inelastic contribution to the diffuse scattering intensity I_{XRD} in Figs. 3(c) and 3(d). Hence, detected increases

in I_{XRD} and total I_{IXS} towards 150 K are almost entirely due to a growing *elastic* contribution. A complementary signature of this growing elastic scattering contribution is the increasing height of the central peaks in the IXS spectra in Figs. 4(a) and 4(b). Thus the displacive and phonon-driven component of the structural phase transition at 150 K seems to be complemented by an additional order-disorder-type component with quasistatic fluctuations while approaching the transition temperature [37,89,90]. Both elastic and inelastic IXS intensities at W rapidly decay to zero below 150 K [Fig. 3(d)]. The large intensity of the superstructure reflections at T did not allow an analogous collection of IXS spectra down to temperatures below 160 K [Fig. 3(c)]. Still, a further increase of the elastic intensity towards lower temperatures in the company of a reduction of the inelastic intensity to zero may be expected.

C. X-ray diffraction

Our diffuse and inelastic x-ray scattering investigations thus point out a completion of the phonon softening process in Sc_3CoC_4 at ~150 K, i.e., already at the lower end of the temperature regime of stage (i) defined in Sec. III. This finding, however, raises questions regarding the significance of the intermediate temperature regime [stage (ii)] of the HT-LT transition extending from 150 K towards anomalies in superstructure reflection intensities, electrical resistivity, and magnetization at ~80 K [47–51,57].

One possible explanation for the second anomaly can be derived from the fact that not only may the Peierls-type structural distortion in Sc_3CoC_4 be crystallographically described using a monoclinic unit cell with doubled volume with respect to the orthorhombic unit cell of the HT-phase structural model, but also, alternatively, a description by a modulation of the orthorhombic HT phase structural model
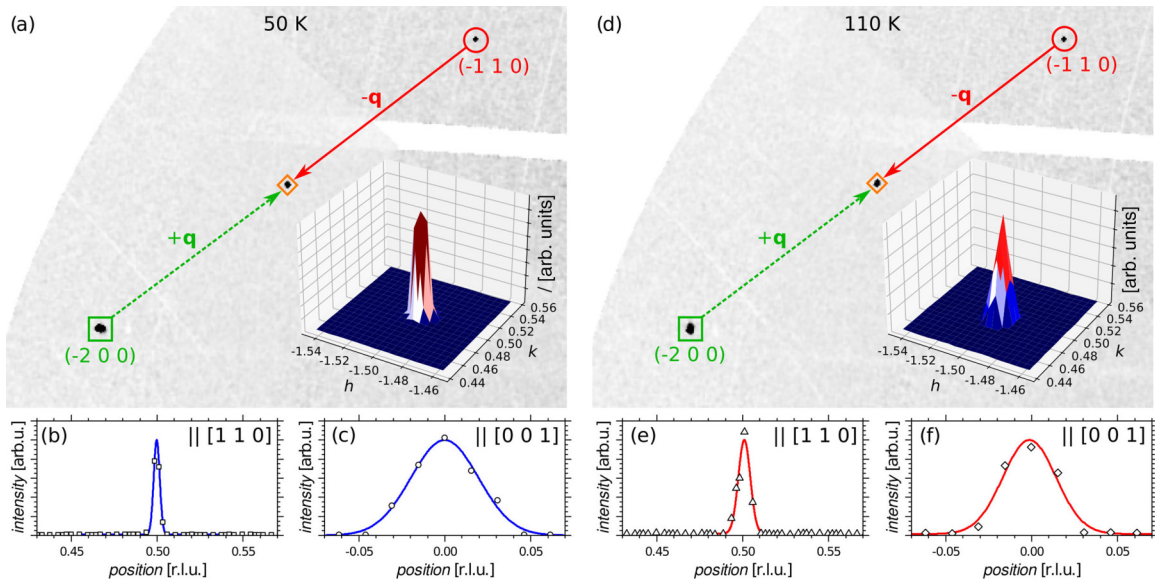
FIG. 6. Exemplary sections of reconstructed ($hk0$) reciprocal-space planes at (a) 50 K and (d) 110 K containing the superstructure reflection $(-1.5, 0.5, 0)$ (orange diamond) and its corresponding main reflections (red circle and green square). Three-dimensional intensity profiles of the superstructure reflection in the reconstructed ($hk0$) planes are given as insets at the lower right. One-dimensional intensity profiles of the superstructure reflection along directions [110] and [001] are shown in (b) and (c) (50 K) and (e) and (f) (110 K). Note that the indexing of reflections refers to the orthorhombic HT-phase unit cell of Sc_3CoC_4.

is possible with modulation wave vectors [91] $\mathbf{q} = [0.5 + \delta, \pm(0.5 + \epsilon), 0]$ and potential lattice incommensurabilities δ and ϵ [50]. This suggests that we draw analogies between Sc_3CoC_4 and other structurally low-dimensional materials such as tetrathiafulvalenium-tetracyanoquinodimethanide (TTF-TCNQ) [34,92], $1T$-TaS_2 [38,39,93,94], and $2H$-$TaSe_2$ [38,95,96], where first-order-like changes [97,98] in superstructure reflection intensities, electrical resistivity, and magnetic susceptibility have been found to correspond to a lock-in transition from an incommensurately to a commensurately modulated phase. Such a potential lock-in transition from an incommensurately modulated phase in the temperature regime of stage (ii) (80 K $\leqslant T \leqslant$ 150 K) to a commensurately modulated phase in the temperature regime of stage (iii) ($T < 80$ K) would consequently be linked to a decrease in the superstructure reflection profile widths along [110] or [1$\bar{1}$0] upon cooling below 80 K. High-resolution synchrotron XRD experiments on a single-crystalline needle of Sc_3CoC_4, however, give no substantial evidence of a potential lattice incommensurability of the structural distortion: A comparison of ($hk0$) reciprocal-space planes and line profiles reconstructed from XRD data collected at ∼50 K [example in Figs. 6(a)–6(c)] and 110 K [example in Figs. 6(d)–6(f)] does not reveal significant temperature-dependent changes in superstructure reflection profiles. For the remaining analysis of XRD results, the structure of Sc_3CoC_4 will therefore be assumed to be fully commensurate independent of temperature.

To gain more insight into the temperature-dependent progression of structural changes between the temperature regimes of stages (ii) and (iii), we performed additional x-ray diffraction experiments covering the whole temperature range between 300 and 10 K with a narrow temperature spacing of ∼10 K (see Fig. 7, as well as Sec. SVI of the Supplemental Material [59] and Refs. [99,100] therein). These demon-

strate, in line with earlier findings [51], that the first atomic displacements breaking the HT-phase space group symmetry *Immm* occur already at a temperature of ∼180 K [Fig. 7(a)], i.e., at the lower end of the temperature regime of stage (i) of the HT-LT transition [101]. This correlates well with the onset temperature of the quasielastic central peak in the IXS spectra in Fig. 4. XRD data collected at lower temperatures down to ∼10 K, i.e., in the intermediate temperature regime [stage (ii)] as well as in the final temperature regime [stage (iii)], may invariably be described by space group $C2/m$ (No. 12 [58]) without any apparent signs of a further global symmetry reduction.

The temperature-dependent emergence of Co-Co (Sc1-Sc1) dimers in the Co (Sc1) chains as a main feature of the Peierls-type structural distortion (see Sec. III and Refs. [46–52]) is demonstrated by the plot of Co-Co (blue circles) and Sc1-Sc1 bond distances (magenta squares) along axes a_{HT} and b_{HT}, respectively, in Fig. 7(a). Below ∼180 K, adjacent long and short Co-Co (Sc1-Sc1) contacts can be identified in the Co (Sc1) chains of refined structural models. The following temperature range between 180 and 80 K, which approximately coincides with the intermediate temperature regime [stage (ii)] of the HT-LT transition defined in Sec. III, is then characterized by a gradual and continuous growth of the bond length differences between long and short contacts. Closer inspection of Fig. 7(a) reveals two kinks in the temperature dependencies of the bond lengths at ∼150 and 100 K delimiting a region of reduced slope. Notably, the first temperature is identical to the completion temperature of the phonon softening process observed in the IXS investigations above (Fig. 4). Cooling of the sample to temperatures below ∼80 K, i.e., stage (iii) of the transition, finally results in a saturation of the bond length differences between long and short atomic contacts. As becomes evident
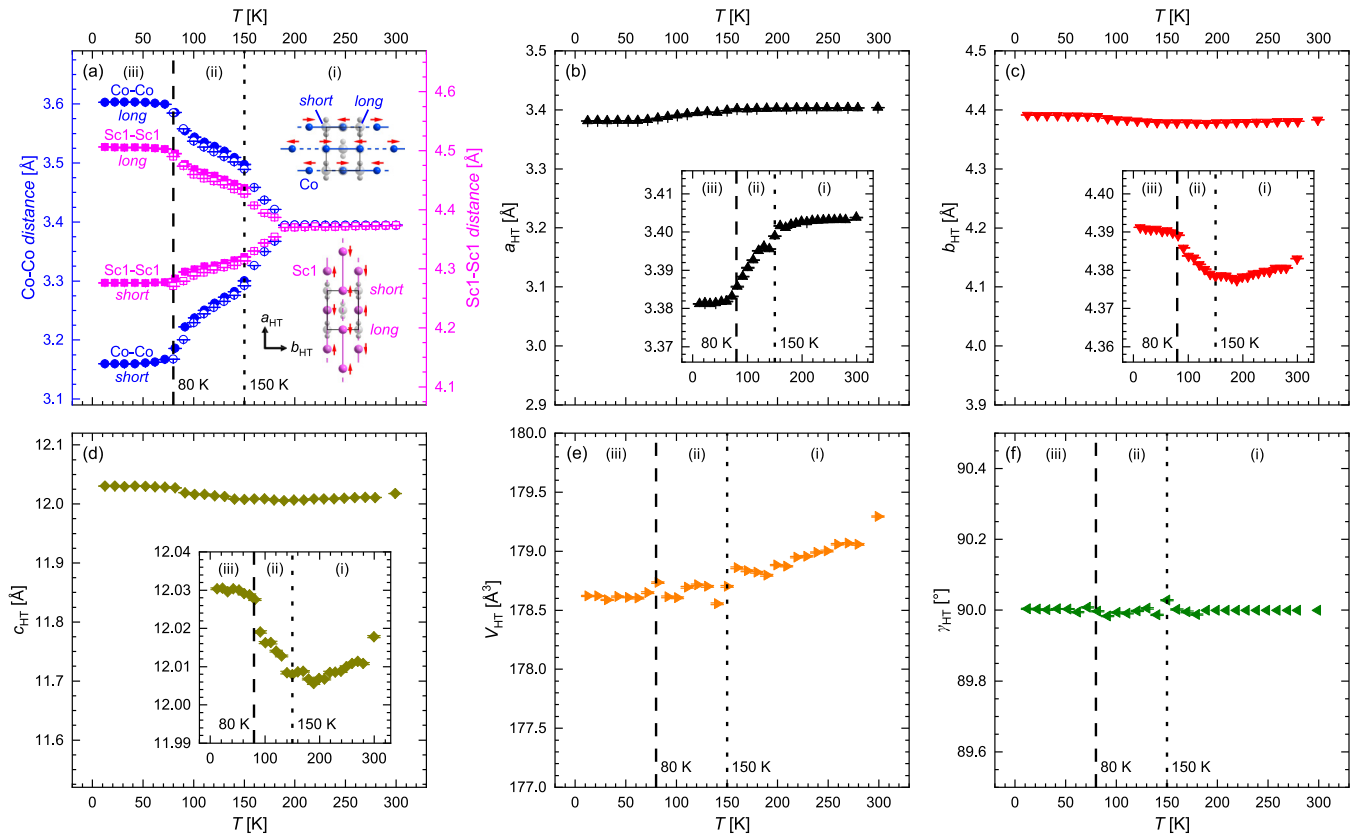
FIG. 7. Overview of temperature-dependent structural changes as observed in single-crystal XRD studies of Sc_3CoC_4. (a) Displacements of Co and Sc1 atoms lead to a dimerization in linear chains along the a_{HT} and b_{HT} axes and to the formation of alternating short and long Co-Co and Sc1-Sc1 atomic distances [sketched in the insets in (a)]. Changes in the unit cell parameters (b) a_{HT}, (c) b_{HT}, and (d) c_{HT} are small in comparison to the atomic displacements in (a) (plots using a smaller scale are shown as insets) and partially compensate each other, so that only a minor variation of the cell volume V_{HT} (e) results. At the same time, the cell angle γ_{HT} (f) deviates only insignificantly from $90°$ indicating the absence of significant monoclinic shearing of the orthorhombic HT-phase unit cell. Note that for clarity, all structural changes are referred to the orthorhombic reference frame of the HT-phase structural model (see text and Ref. [102] for further details). Furthermore, structural data have been compiled from two different measurement runs using laboratory-scale instrumental setups 1 and 2 described in Sec. II (open and filled symbols, respectively).

from Fig. S23 in the Supplemental Material [59], the Co-C and C-C bond lengths along the $[Co(C_2)_2]_\infty$ ribbons remain largely unaffected by the structural changes below 180 K: While the C-C bond lengths appear to be temperature independent within the limits of experimental error, a slight temperature-dependent increase in the Co-C bond lengths is found between 180 and 80 K. This tendency towards longer Co-C bond lengths may be attributed to the growing cobalt atomic displacements along $\pm a_{HT}$ perpendicular to the ribbon direction b_{HT}. In summary, the obtained temperature dependencies of bond distances [Fig. 7(a)] and lattice parameters [Figs. 7(b)–7(d)] clearly support the three-stage picture of the HT-LT transition in Sc_3CoC_4: After its appearance at $\sim$180 K [i.e., the lower bound of stage (i)] the Peierls-type structural distortion remains subject to ongoing and continuous changes throughout the intermediate temperature regime [stage (ii)] between 150 and 80 K and only settles into its final state in the temperature regime of stage (iii) below $\sim$80 K.

These structural changes during the temperature regimes of stages (i), (ii), and (iii) also affect the electronic band structure of Sc_3CoC_4 at the Fermi energy E_F (Fig. 8). Density functional theory (DFT) studies based on temperature-dependent

geometries from the present XRD experiments indicate that in the HT-phase structure at room temperature, E_F is located close to a peak in the total density of states (DOS). This peak is subject to an ongoing splitting during the progression of the Peierls-type structural distortion. Between RT and 100 K the DOS at E_F is reduced by $\sim$15% from 6.76 states/eV [Fig. 8(a)] to 5.72 states/eV [Fig. 8(b)]. A further and more significant reduction (by $\sim$32%) from 5.72 to 3.92 states/eV appears between 100 and 12 K [Fig. 8(c)], so that the overall reduction amounts to $\sim$42%. Qualitatively, the course of the DOS near E_F changes from a peaklike feature at RT to a local minimum at 12 K. These findings can be correlated with the experimentally observed rises in the electrical resistivity and drops in the magnetic susceptibility at $\sim$150 and 80 K [47–49,51,57].

In a next step, the additional analysis of temperature-dependent unit cell parameter changes allows for a decoupling of the local structural changes in terms of the bond distances from the temperature-dependent deformations of the lattice. A back-transformation of cell parameters corresponding to the monoclinic reference frame of the LT-phase structural models to the orthorhombic reference frame of the HT-phase
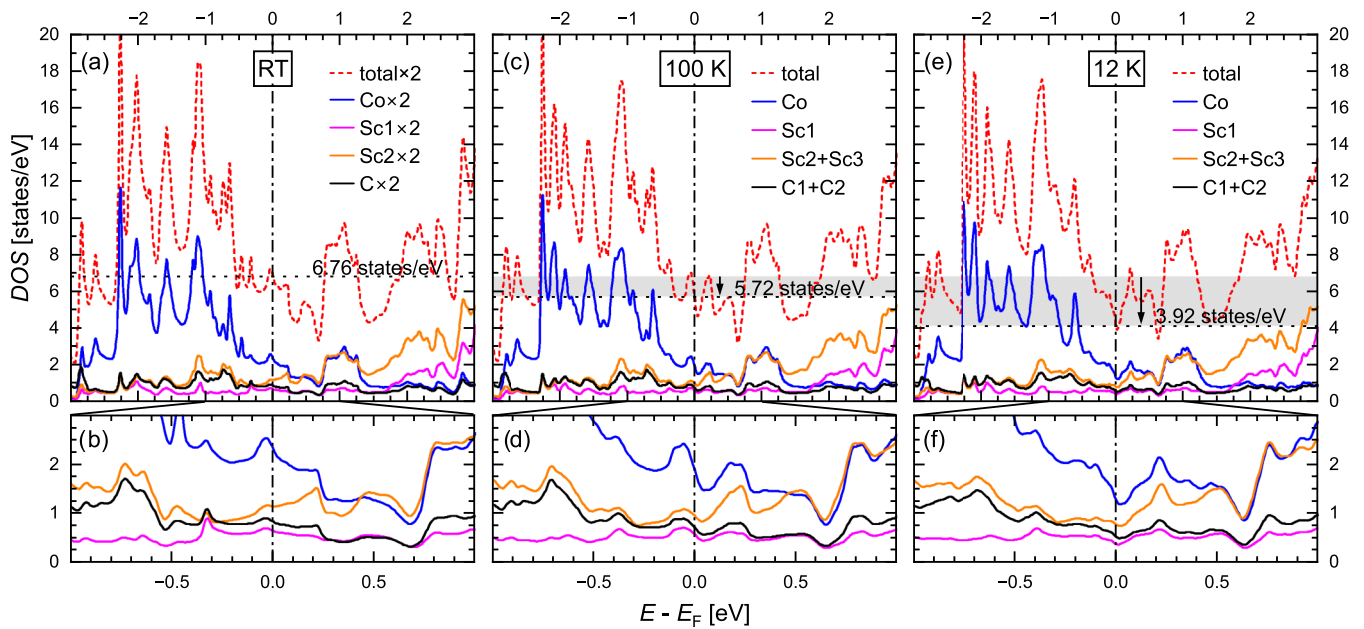
FIG. 8. Changes in the total (dashed lines) and site-projected DOS (solid lines) as a consequence of the variation of lattice parameters and fractional atomic coordinates upon cooling from RT [(a) and (b)] to 100 K [(c) and (d)] and 12 K [(e) and (f)]. Enlarged views of the site-projected DOS around the Fermi level (E_F) are given in (b), (d), and (f). Note that the pairs of atomic sites Sc2-Sc3 and C1-C2 in the monoclinic LT-phase structure of Sc_3CoC_4 (space group $C2/m$, No. 12 [58]) are equivalent to atomic sites Sc2 and C in the orthorhombic HT-phase structure (space group $Immm$, No. 71 [58]; see also the Bärnighausen diagram in Fig. S1 of the Supplemental Material [59]).

structural models (further information and plots of the original monoclinic cell parameters are available in Sec. SVI of the Supplemental Material [59]) reveals [Figs. 7(b)–7(f)] that the unit cell retains its orthorhombic geometry throughout the investigated temperature range between 300 and 10 K. The symmetry reduction from orthorhombic space group $Immm$ to monoclinic space group $C2/m$ in the HT-LT transition of Sc_3CoC_4 is therefore mainly reflected by changes in the relative atomic positions and not by a deformation of the unit cell shape. This secondary role of lattice parameter changes in the structural modifications is also supported by a quantitative comparison of the temperature-dependent changes of cell parameters a_{HT}, b_{HT}, and c_{HT} (order of magnitude $\sim 10^{-2}$ Å) and of Co-Co and Sc1-Sc1 bond distances (order of magnitude $\sim 10^{-1}$ Å).

Still, unit cell parameters a_{HT} parallel to the cobalt atom chains [Fig. 7(b)], b_{HT} parallel to the $[Co(C_2)_2]_\infty$ ribbons [Fig. 7(c)], and c_{HT} parallel to the stacking direction of the quasi-2D layers [Fig. 7(d)] display interesting temperature dependencies which can also be reconciled with a three-stage model of the HT-LT transition of Sc_3CoC_4 at ambient pressure (Sec. III). In the final stage [stage (iii)] of the HT-LT transition below ~ 80 K, cell parameters and cell volume [Fig. 7(e)] reach nearly constant values. Above this temperature, a continued decrease upon cooling is only found for a_{HT} [Fig. 7(b)]. Conversely, cell parameters b_{HT} [Fig. 7(c)] and c_{HT} [Fig. 7(d)] show a decreasing tendency down to ~ 180 K followed by temperature regimes of weaker (b_{HT}) or stronger (c_{HT}) negative thermal expansion. Despite the occurrence of negative thermal expansion along cell axes b_{HT} and c_{HT}, an overall decreasing trend is found for the cell volume V_{HT} [Fig. 7(e)] between 300 K and its saturation at 80 K interrupted only by anomalies centered at 150 and 80 K [102]. It should further

be noted that although the temperature dependencies of cell parameters, cell volume, and even cell angles consistently show minor anomalies close to the onset of the temperature regime of stage (ii) at ~ 150 K [Figs. 7(b)–7(f)], tracking of high-angle reflection positions in 1 K temperature increments demonstrated that the associated lattice deformations have a continuous and second-order character (further details can be found in Sec. SV of the Supplemental Material [59]).

This, however, may not be the case for the lattice deformations close to the transition to the temperature regime of stage (iii) at ~ 80 K: Especially c_{HT} [Fig. 7(d)] displays a comparatively large steplike change before settling at a nearly constant value for temperatures below 80 K. This finding may be one aspect of a subtle interplay between the ongoing structural changes during the intermediate stage [stage (ii)] of the HT-LT transition between 150 and 80 K, the crystal stress-strain state, and the emergence of systematic (pseudo)merohedral twinning. The loss of a mirror plane perpendicular to the a_{HT} axis in the $t2$ step of the symmetry reduction from space group $Immm$ to space group $C2/m$ results in the occurrence of two distinct twin domain states with different orientations (see Sec. III and Refs. [46–52]). The ongoing structural changes during the temperature regime of stage (ii) may thus lead to a continuous variation of the crystal stress-strain state due to the formation of a twin domain structure of the crystals. Only when the final state of the Peierls-type distorted LT-phase structure is reached in the temperature regime of stage (iii) below 80 K does this twin domain structure settle into a final state which likely minimizes the overall crystal strain energy.

Experimental evidence supporting the hypothesis of a buildup of stress in the crystal during the temperature regime of stage (ii) and its minimization upon the transition into the temperature regime of stage (iii) is provided by the observa-

tion of a transient broadening or even splitting of selected high-angle main *and* superstructure reflections observed in our high-resolution reciprocal-space mapping experiments. This broadening might be caused by minor lattice mismatches between adjacent twin domains at the local scale. It consistently appears upon cooling towards 80 K [the temperature regime of stage (ii) of the HT-LT transition] and vanishes upon further cooling to 50 K (the temperature regime of stage (iii); see the temperature-dependent resolution histograms and the reconstructed reciprocal-space planes for high-angle reflections in Figs. S21 and S22 of the Supplemental Material [59]). It should be emphasized that the observed broadening or splitting is different from the expected peak broadening pattern discussed above for a potential incommensurate-to-commensurate lock-in transition: On the one hand, the observed splitting tends to increase upon cooling towards 80 K (Fig. S21 of the Supplemental Material [59]) contrasting with the expected decreasing trend of lattice incommensurability towards the lock-in transition temperature [98,103], and on the other hand, main Bragg *and* superstructure reflections are broadened or split in the same manner (*vide supra*), which should not be the case for a lock-in transition either.

Future investigations of the local crystal domain structure and the arrangement of twin domains in the needlelike Sc_3CoC_4 samples (e.g., using total x-ray and neutron scattering techniques, transmission electron microscopy, or x-ray topography [82]) may thus help to gain an even deeper understanding of the processes leading from the intermediate stage [stage (ii)] to the final stage [stage (iii)] of the Peierls-type structural distortion of Sc_3CoC_4.

V. DISCUSSION

As shown above and in line with earlier investigations [50], our experimental data allow us to define three stages in the progression of Sc_3CoC_4 from the HT-phase structure to the final LT-phase structure: A combination of a phonon softening and an order-disorder-type mechanism brings samples of the compound from the HT phase [stage (i)] to an intermediate phase [stage (ii)]. The transition temperature between stages (i) and (ii) at around 150 K is characterized by a vanishing frequency of the soft T_1^+ phonon mode and by an emerging displacive modulation of cobalt and scandium atomic positions that reduces the space group symmetry from $Immm$ to $C2/m$. Further cooling to temperatures below 150 K leads to a gradual growth of the symmetry-breaking atomic displacements and finally to their saturation in the final LT phase [stage (iii)] below $\sim$80 K without any hints of an incommensurability of the structural modulation or a further global reduction of space group symmetry.

The investigated transition-metal carbide Sc_3CoC_4 belongs to a larger class of materials featuring an interplay between a structural phase transition at higher temperatures and a superconducting phase transition at lower temperatures. Among the best-studied representatives are the charge-density-wave (CDW) compounds [34–39] and the binary A15 compounds [104,105] displaying low-dimensional and three-dimensional structural motifs, respectively. Similar to our results for Sc_3CoC_4 above, many of these superconducting materials have been found to undergo phonon

softening processes towards their structural phase transition temperatures [34,61,89,90,95,96,104–114]. Furthermore, the structural and superconducting phase transitions in Sc_3CoC_4, CDWs, and A15 compounds are susceptible to a manipulation by means of applied strain or hydrostatic pressure [34–36,40–44,51,52,57,104,110,115–117].

In the A15 materials V_3Si ($T_c = 17.1$ K [118]) and Nb_3Sn ($T_c = 18.1$ K [119]), the onset of superconductivity is preceded by cubic-to-tetragonal structural transformations from space group $Pm\bar{3}n$ [120–122] (No. 223 [58]) to space group $P4_2/mmc$ [104,115,123–127] (No. 131 [58]) at $\sim$20 K (V_3Si) [123,126] and 45 K (Nb_3Sn) [115,125,126]. While often referred to as martensitic, these phase transitions are of weak first order and show only a little resemblance to the strongly first-order martensitic transformations in steels [79,104,113,115,124,126,128–132]. Cooling towards their structural transition temperature thus leads to the appearance of diffuse scattering at the positions of formally extinct reflections as a consequence of pretransitional structural fluctuations [133] and to the softening of phonon modes close to the Γ point of the phonon dispersion relation [104–106,108–110,113,114].

In line with the condensation of a zone-center phonon mode [113,114], the symmetry reduction in V_3Si and Nb_3Sn from space group $Pm\bar{3}n$ to space group $P4_2/mmc$ involves only a *translationengleiche* (*t*3) step and no doubling of the unit cell volume [105,123–125] like in the HT-LT transition of Sc_3CoC_4. The structural changes due to the tetragonal distortion of the A15 compounds therefore do not allow an alternative description by a commensurate or incommensurate displacive modulation of the cubic parent phase. Nevertheless, chains of vanadium or niobium atoms with two atoms per unit cell can be identified in the crystal structure of V_3Si and Nb_3Sn that undergo a Peierls-like dimerization even in the absence of a unit cell enlargement [104,127,134]. DFT studies by Sadigh and Ozoliņš [113] point out that this process also results in the splitting of a sharp DOS peak at the Fermi level of Nb_3Sn and the reduction of DOS(E_F) by $\sim$25%.

In comparison to the atomic displacements of the cobalt ($\sim$0.11 Å) and scandium atoms ($\sim$0.06 Å) during the Peierls-type structural distortion of Sc_3CoC_4, however, the atomic displacements of the vanadium (0.0015 Å) [133] or niobium atoms (0.016 Å) [115] during the cubic-to-tetragonal phase transitions of V_3Si and Nb_3Sn remain rather small [104,115,123,125,126,133]. Atomic displacements larger than those in the A15 materials and on a level similar to those in Sc_3CoC_4 have been observed for the Peierls-type structural distortions in low-dimensional charge-density-wave materials (e.g., up to 0.09 Å for the tantalum atoms in $2H$-$TaSe_2$ [95,96] and $(TaSe_4)_2I$ [112]). Furthermore, the resulting low-temperature phase structures in CDW compounds such as the quasi-one-dimensional $K_{0.3}MoO_3$ [34,89,111,135], $K_2Pt(CN)_4Br_{0.3} \cdot 3.2\, D_2O$ (KCP) [34,107], $NbSe_3$ [34,136], $ZrTe_3$ [61,90], and $(TaSe_4)_2I$ [112], as well as the quasi-two-dimensional $2H$-$TaSe_2$ [96], may be described as displacively modulated variants of a parent structure with an incommensurate or commensurate **q** vector. Even above the actual transition temperature into the modulated phase, all of the aforementioned materials already show a regime of structural fluctuations that is characterized by the

presence of distinct diffuse scattering and the critical growth of an elastic central peak in inelastic x-ray or neutron scattering spectra [34,61,89,90,96,107,111,112,135,136]. Yet only $K_{0.3}MoO_3$ [34,89,111] and $ZrTe_3$ [61,90] are affected by a simultaneous phonon softening of a non-zone-center phonon mode close to zero energy in analogy to Sc_3CoC_4. Phonon softening in the other CDW compounds is weaker, as in KCP [34,107], $(TaSe_4)_2I$ [112], and $2H$-$TaSe_2$ [95,96], or even completely absent, as in $NbSe_3$ [136].

The comparison with the A15 and CDW superconductors thus illustrates the extraordinary nature of the two-step structural phase transition in Sc_3CoC_4 at ambient pressure. Isolated characteristics such as the existence of a phonon softening mechanism or the emergence of a displacive structural modulation may also be identified in the reference compounds. Yet the HT-LT transition in Sc_3CoC_4 stands out by its progression from an orthorhombic HT phase via a monoclinic intermediate phase to a final LT phase with *identical* space group symmetry. Unlike the CDW compounds the Peierls-type atomic displacements appearing in the intermediate phase are *not* characterized by a significant lattice incommensurability, but by a temperature-dependent and continuous growth towards a constant value in the final LT phase.

VI. CONCLUSION

To summarize, we obtained information about the progression of the structurally low-dimensional superconductor Sc_3CoC_4 towards its Peierls-type distorted low-temperature (LT) phase using temperature-dependent x-ray diffraction and inelastic x-ray scattering experiments on high-quality single-crystalline samples. In support of our previous proposition [50], we identify a soft branch along the high-symmetry path W–T of the phonon dispersion that drives significant dynamic and LT-phase-like displacements of cobalt and scandium atoms already at room temperature. All phonon modes in the branch show further softening upon cooling, but only

the T_1^+ phonon mode reaches zero frequency at $\sim$150 K and thus determines the $C2/m$ space group symmetry of the final LT phase. Yet we also show that a purely displacive and phonon-softening-driven picture of the structural distortion in Sc_3CoC_4 is not sufficient. It has to be complemented by an additional order-disorder-type contribution involving quasistatic pretransitional fluctuations of the crystal structure.

The observed completion of the phonon softening and ordering processes in Sc_3CoC_4 already at $\sim$150 K brings into focus the significance of anomalies in the temperature dependencies of lattice parameters, electrical resistivity, and magnetization at $\sim$80 K [47–49,51,57]. In contrast to a number of charge-density-wave compounds [34,38,38,39,92–96] we could not associate these anomalies with a lock-in transition from an incommensurate to a commensurate structural modulation. Instead, the temperature regime between 150 and 80 K was found to correspond to an accumulation of gradual changes in lattice parameters and atomic positions. It is only below a temperature of 80 K that these parameters settle into their final and constant states without a further reduction of space group symmetry. We may thus speculate about the existence of a lattice relaxation process at $\sim$80 K that leaves the overall atomic displacement pattern due to the Peierls-type structural distortion intact but reduces the crystal strain energy.

Raw data from the IXS, DS, and reflection position tracking experiments are available from the corresponding author upon reasonable request.

[1] A. S. Alexandrov, *Theory of Superconductivity*, 1st ed. (Institute of Physics, Bristol, UK, 2003), Chap. 2, pp. 33–72.

[2] D. Duan, H. Yu, H. Xie, and T. Cui, *Ab initio* approach and its impact on superconductivity, J. Supercond. Novel Magn. **32**, 53 (2019).

[3] B. Lilia, R. Hennig, P. Hirschfeld, G. Profeta, A. Sanna, E. Zurek, W. E. Pickett, M. Amsler, R. Dias, M. I. Eremets, C. Heil, R. J. Hemley, H. Liu, Y. Ma, C. Pierleoni, A. N. Kolmogorov, N. Rybin, D. Novoselov, V. Anisimov, A. R. Oganov *et al.*, The 2021 room-temperature superconductivity roadmap, J. Phys.: Condens. Matter **34**, 183002 (2022).

[4] D. Duan, Y. Liu, F. Tian, D. Li, X. Huang, Z. Zhao, H. Yu, B. Liu, W. Tian, and T. Cui, Pressure-induced metallization of dense $(H_2S)_2H_2$ with high-T_c superconductivity, Sci. Rep. **4**, 6968 (2014).

[5] A. P. Drozdov, M. I. Eremets, I. A. Troyan, V. Ksenofontov, and S. I. Shylin, Conventional superconductivity at 203 Kelvin at high pressures in the sulfur hydride system, Nature (London) **525**, 73 (2015).

[6] H. Liu, I. I. Naumov, R. Hoffmann, N. W. Ashcroft, and R. J. Hemley, Potential high-T_c superconducting lanthanum and yttrium hydrides at high pressure, Proc. Natl. Acad. Sci. USA **114**, 6990 (2017).

[7] A. P. Drozdov, P. P. Kong, V. S. Minkov, S. P. Besedin, M. A. Kuzovnikov, S. Mozaffari, L. Balicas, F. F. Balakirev, D. E. Graf, V. B. Prakapenka, E. Greenberg, D. A. Knyazev, M. Tkacz, and M. I. Eremets, Superconductivity at 250 K in lanthanum hydride under high pressures, Nature (London) **569**, 528 (2019).

[8] J. D. Jorgensen, D. G. Hinks, and G. P. Felcher, Lattice instability and superconductivity in the Pb, Sn, and Ba Chevrel phases, Phys. Rev. B **35**, 5365(R) (1987).

[9] Y. S. Yao, R. P. Guertin, D. G. Hinks, J. Jorgensen, and D. W. Capone II, Superconductivity of divalent Chevrel phases at very high pressures, Phys. Rev. B **37**, 5032 (1988).

[10] O. Peña, Chevrel phases: Past, present and future, Phys. C (Amsterdam) **514**, 95 (2015).

[11] K. Yvon, On the lattice instabilities in Chevrel phases, Solid State Commun. **25**, 327 (1978).

[12] T. Nomura, S. W. Kim, Y. Kamihara, M. Hirano, P. V. Sushko, K. Kato, M. Takata, A. L. Shluger, and H. Hosono, Tetragonal-orthorhombic phase transition and F-doping effects on the crystal structure in the iron-based high-T_c superconductor LaFeAsO, J. Phys. Soc. Jpn. **77**, 32 (2008).

[13] T. Nomura, S. W. Kim, Y. Kamihara, M. Hirano, P. V. Sushko, K. Kato, M. Takata, A. L. Shluger, and H. Hosono, Crystallographic phase transition and high-T_c superconductivity in LaFeAsO:F, Supercond. Sci. Technol. **21**, 125028 (2008).

[14] M. Rotter, M. Pangerl, M. Tegel, and D. Johrendt, Superconductivity and crystal structures of $(Ba_{1-x}K_x)Fe_2As_2$ ($x = 0–1$), Angew. Chem., Int. Ed. **47**, 7949 (2008).

[15] T. M. McQueen, A. J. Williams, P. W. Stephens, J. Tao, Y. Zhu, V. Ksenofontov, F. Casper, C. Felser, and R. J. Cava, Tetragonal-to-Orthorhombic Structural Phase Transition at 90 K in the Superconductor $Fe_{1.01}Se$, Phys. Rev. Lett. **103**, 057002 (2009).

[16] D. Johrendt, Structure-property relationships of iron arsenide superconductors, J. Mater. Chem. **21**, 13726 (2011).

[17] G. Ghiringhelli, M. Le Tacon, M. Minola, S. Blanco-Canosa, C. Mazzoli, N. B. Brookes, G. M. De Luca, A. Frano, D. G. Hawthorn, F. He, T. Loew, M. Moretti Sala, D. C. Peets, M. Salluzzo, E. Schierle, R. Sutarto, G. A. Sawatzky, E. Weschke, B. Keimer, and L. Braicovich, Long-range incommensurate charge fluctuations in (Y, Nd)$Ba_2Cu_3O_{6+x}$, Science **337**, 821 (2012).

[18] S. Blanco-Canosa, A. Frano, E. Schierle, J. Porras, T. Loew, M. Minola, M. Bluschke, E. Weschke, B. Keimer, and M. Le Tacon, Resonant x-ray scattering study of charge-density wave correlations in $YBa_2Cu_3O_{6+x}$, Phys. Rev. B **90**, 054513 (2014).

[19] M. Hücker, N. B. Christensen, A. T. Holmes, E. Blackburn, E. M. Forgan, R. Liang, D. A. Bonn, W. N. Hardy, O. Gutowski, M. v. Zimmermann, S. M. Hayden, and J. Chang, Competing charge, spin, and superconducting orders in underdoped $YBa_2Cu_3O_y$, Phys. Rev. B **90**, 054514 (2014).

[20] J. Chang, E. Blackburn, A. T. Holmes, N. B. Christensen, J. Larsen, J. Mesot, R. Liang, D. A. Bonn, W. N. Hardy, A. Watenphul, M. v. Zimmermann, E. M. Forgan, and S. M. Hayden, Direct observation of competition between superconductivity and charge density wave order in $YBa_2Cu_3O_{6.67}$, Nat. Phys. **8**, 871 (2012).

[21] S. Blanco-Canosa, A. Frano, T. Loew, Y. Lu, J. Porras, G. Ghiringhelli, M. Minola, C. Mazzoli, L. Braicovich, E. Schierle, E. Weschke, M. Le Tacon, and B. Keimer, Momentum-Dependent Charge Correlations in $YBa_2Cu_3O_{6+\delta}$ Superconductors Probed by Resonant X-Ray Scattering: Evidence for Three Competing Phases, Phys. Rev. Lett. **110**, 187001 (2013).

[22] G. Fabbris, M. Hücker, G. D. Gu, J. M. Tranquada, and D. Haskel, Local structure, stripe pinning, and superconductivity in $La_{1.875}Ba_{0.125}CuO_4$ at high pressure, Phys. Rev. B **88**, 060507(R) (2013).

[23] S. M. Souliou, H. Gretarsson, G. Garbarino, A. Bosak, J. Porras, T. Loew, B. Keimer, and M. Le Tacon, Rapid suppression of the charge density wave in $YBa_2Cu_3O_{6.6}$ under hydrostatic pressure, Phys. Rev. B **97**, 020503(R) (2018).

[24] H.-H. Kim, S. M. Souliou, M. E. Barber, E. Lefrançois, M. Minola, M. Tortora, R. Heid, N. Nandi, R. A. Borzi, G. Garbarino, A. Bosak, J. Porras, T. Loew, M. König, P. J. W.

Moll, A. P. Mackenzie, B. Keimer, C. W. Hicks, and M. Le Tacon, Uniaxial pressure control of competing orders in a high-temperature superconductor, Science **362**, 1040 (2018).

[25] H.-H. Kim, E. Lefrançois, K. Kummer, R. Fumagalli, N. B. Brookes, D. Betto, S. Nakata, M. Tortora, J. Porras, T. Loew, M. E. Barber, L. Braicovich, A. P. Mackenzie, C. W. Hicks, B. Keimer, M. Minola, and M. Le Tacon, Charge Density Waves in $YBa_2Cu_3O_{6.67}$ Probed by Resonant X-Ray Scattering under Uniaxial Compression, Phys. Rev. Lett. **126**, 037002 (2021).

[26] G. Marini, A. Sanna, C. Pellegrini, C. Bersier, E. Tosatti, and G. Profeta, Superconducting Chevrel phase $PbMo_6S_8$ from first principles, Phys. Rev. B **103**, 144507 (2021).

[27] V. Palmisano, S. Agrestini, G. Campi, M. Filippi, L. Simonelli, M. Fratini, A. Bianconi, S. De Negri, M. Giovannini, A. Saccone, A. N. Fitch, M. Brunelli, and I. Margiolaki, Anomalous thermal expansion in superconducting $Mg_{1-x}Al_xB_2$ system, J. Supercond. **18**, 737 (2005).

[28] S. Y. Wu, P.-H. Shih, J.-Y. Ji, T.-S. Chan, and C. C. Yang, Direct observation of charge re-distribution in a MgB_2 superconductor, Supercond. Sci. Technol. **29**, 045001 (2016).

[29] J. Langmann, H. Kepenci, G. Eickerling, K. Batke, A. Jesche, M. Xu, P. Canfield, and W. Scherer, Experimental x-ray charge-density studies—A suitable probe for superconductivity? A case study on MgB_2, J. Phys. Chem. A **126**, 8494 (2022).

[30] B. Lachal, R. Baillif, A. Junod, and J. Muller, Structural instabilities of Chevrel phases: The alkaline earth molybdenum sulphide series, Solid State Commun. **45**, 849 (1983).

[31] Ø. Fischer, Chevrel phases: Superconducting and normal state properties, Appl. Phys. **16**, 1 (1978).

[32] J. D. Jorgensen and D. G. Hinks, Low temperature structural distortion in the high T_c Chevrel-phase superconductors $PbMo_6S_8$ and $SnMo_6S_8$, Solid State Commun. **53**, 289 (1985).

[33] J. Paglione and R. L. Greene, High-temperature superconductivity in iron-based materials, Nat. Phys. **6**, 645 (2010).

[34] J. P. Pouget and R. Comes, The CDW transition, structural studies, in *Charge Density Waves in Solids*, Modern Problems in Condensed Matter Sciences Vol. 25, 1st ed., edited by L. P. Gor'kov and G. Grüner (North-Holland, Amsterdam, 1989), Chap. 3, pp. 85–136.

[35] A. M. Gabovich, A. I. Voitenko, and M. Ausloos, Charge-and spin-density waves in existing superconductors: Competition between Cooper pairing and Peierls or excitonic instabilities, Phys. Rep. **367**, 583 (2002).

[36] P. Monceau, Electronic crystals: An experimental overview, Adv. Phys. **61**, 325 (2012).

[37] J.-P. Pouget, The Peierls instability and charge density wave in one-dimensional electronic conductors, C. R. Phys. **17**, 332 (2016).

[38] F. C. Brown, Charge density waves in the transition-metal dichalcogenides: Recent experimental advances, in *Structural Phase Transitions in Layered Transition Metal Compounds*, Physics and Chemistry of Materials with Low-Dimensional Structures Vol. 8, 1st ed., edited by K. Motizuki (Reidel, Dordrecht, 1986), Chap. 4, pp. 267–292.

[39] P. M. Williams, Phase transitions and charge density waves in the layered transition metal dichalcogenides, in *Crystallography and Crystal Chemistry of Materials with Layered Structures*, Physics and Chemistry of Materials with Layered

Structures Vol. 2, 1st ed., edited by F. Lévy (Reidel, Dordrecht, 1976), Chap. 2, pp. 51–92.

[40] C. Berthier, P. Molinié, and D. Jérome, Evidence for a connection between charge density waves and the pressure enhancement of superconductivity in 2*H*-NbSe$_2$, Solid State Commun. **18**, 1393 (1976).

[41] A. F. Kusmartseva, B. Sipos, H. Berger, L. Forró, and E. Tutiš, Pressure Induced Superconductivity in Pristine 1*T*-TiSe$_2$, Phys. Rev. Lett. **103**, 236401 (2009).

[42] Y. Feng, J. Wang, R. Jaramillo, J. van Wezel, S. Haravifard, G. Srajer, Y. Liu, Z.-A. Xu, P. B. Littlewood, and T. F. Rosenbaum, Order parameter fluctuations at a buried quantum critical point, Proc. Natl. Acad. Sci. USA **109**, 7224 (2012).

[43] Y. I. Joe, X. M. Chen, P. Ghaemi, K. D. Finkelstein, G. A. de La Peña, Y. Gan, J. C. T. Lee, S. Yuan, J. Geck, G. J. MacDougall, T. C. Chiang, S. L. Cooper, E. Fradkin, and P. Abbamonte, Emergence of charge density wave domain walls above the superconducting dome in 1*T*-TiSe$_2$, Nat. Phys. **10**, 421 (2014).

[44] U. Dutta, P. S. Malavi, S. Sahoo, B. Joseph, and S. Karmakar, Pressure-induced superconductivity in semimetallic 1*T*-TiTe$_2$ and its persistence upon decompression, Phys. Rev. B **97**, 060503(R) (2018).

[45] B. Rohrmoser, G. Eickerling, M. Presnitz, W. Scherer, V. Eyert, R.-D. Hoffmann, U. C. Rodewald, C. Vogt, and R. Pöttgen, Experimental electron density of the complex carbides Sc$_3$[Fe(C$_2$)$_2$] and Sc$_3$[Co(C$_2$)$_2$], J. Am. Chem. Soc. **129**, 9356 (2007).

[46] C. Vogt, R.-D. Hoffmann, U. C. Rodewald, G. Eickerling, M. Presnitz, V. Eyert, W. Scherer, and R. Pöttgen, High- and low-temperature modifications of Sc$_3$RuC$_4$ and Sc$_3$OsC$_4$– Relativistic effects, structure, and chemical bonding, Inorg. Chem. **48**, 6436 (2009).

[47] W. Scherer, C. Hauf, M. Presnitz, E.-W. Scheidt, G. Eickerling, V. Eyert, R.-D. Hoffmann, U. C. Rodewald, A. Hammerschmidt, C. Vogt, and R. Pöttgen, Superconducitvity in quasi one-dimensional carbides, Angew. Chem., Int. Ed. **49**, 1578 (2010).

[48] W. Scherer, G. Eickerling, C. Hauf, M. Presnitz, E.-W. Scheidt, V. Eyert, and R. Pöttgen, On the interplay between real and reciprocal space properties, in *Modern Charge-Density Analysis*, 1st ed., edited by C. Gatti and P. Macchi (Springer, Dordrecht, 2012), Chap. 10, pp. 359–385.

[49] G. Eickerling, C. Hauf, E.-W. Scheidt, L. Reichardt, C. Schneider, A. Muñoz, S. Lopez-Moreno, A. H. Romero, F. Porcher, G. André, R. Pöttgen, and W. Scherer, On the control parameters of the quasi-one dimensional superconducitvity in Sc$_3$CoC$_4$, Z. Anorg. Allg. Chem. **639**, 1985 (2013).

[50] J. Langmann, C. Haas, E. Wenger, D. Schaniel, W. Scherer, and G. Eickerling, Evidence for a soft phonon mode driven Peierls-type distortion in Sc$_3$CoC$_4$, Phys. Rev. B **102**, 094109 (2020).

[51] J. Langmann, M. Vöst, D. Schmitz, C. Haas, G. Eickerling, A. Jesche, M. Nicklas, A. Lanza, N. Casati, P. Macchi, and W. Scherer, Structure of the superconducting high-pressure phase of Sc$_3$CoC$_4$, Phys. Rev. B **103**, 184101 (2021).

[52] A. Fischer, J. Langmann, M. Vöst, G. Eickerling, and W. Scherer, HTD2 — a single-crystal X-ray diffractometer for combined high-pressure/low-temperature experiments at laboratory scale, J. Appl. Crystallogr. **55**, 1255 (2022).

[53] A. O. Tsokol', O. I. Bodak, and E. P. Marusin, The crystal structure of Sc$_3$CoC$_4$, Sov. Phys. Crystallogr. **31**, 466 (1986).

[54] E.-W. Scheidt, C. Hauf, F. Reiner, G. Eickerling, and W. Scherer, Possible indicators for low dimensional superconductivity in the quasi-1D carbide Sc$_3$CoC$_4$, J. Phys.: Conf. Ser. **273**, 012083 (2011).

[55] C. Zhang, J. S. Tse, K. Tanaka, and H.-Q. Lin, Phonon-mediated superconductivity in quasi-1D Sc$_3$CoC$_4$, Europhys. Lett. **100**, 67003 (2012).

[56] M. He, C. H. Wong, D. Shi, P. L. Tse, E.-W. Scheidt, G. Eickerling, W. Scherer, P. Sheng, and R. Lortz, 1D to 3D dimensional crossover in the superconducting transition of the quasi-one-dimensional carbide superconductor Sc$_3$CoC$_4$, J. Phys.: Condens. Matter **27**, 075702 (2015).

[57] E. Wang, X. Zhu, and H.-H. Wen, Pressure-enhanced superconductivity in quasi-1D cobalt carbide Sc$_3$CoC$_4$, Europhys. Lett. **115**, 27007 (2016).

[58] H. Arnold, M. I. Aroyo, E. F. Bertaut, M. J. Billiet, Y. Buerger, H. Burzlaff, J. D. H. Donnay, W. Fischer, D. S. Fokkema, B. Gruber, T. Hahn, H. Klapper, E. Koch, P. B. Konstantinov, G. A. Langlet, A. Looijenga-Vos, U. Müller, P. M. de Wolff, H. Wondratschek, and H. Zimmermann, in *Space-Group Symmetry*, *International Tables for Crystallography Vol. A*, 1st ed., edited by T. Hahn (International Union of Crystallography, Chester, UK, 2006).

[59] See Supplemental Material at http://link.aps.org/supplemental/10.1103/PhysRevB.108.115414 for information on the investigated samples and details of the inelastic x-ray scattering, diffuse scattering, and x-ray diffraction experiments.

[60] M. Krisch and F. Sette, Inelastic x-ray scattering from phonons, in *Light Scattering in Solids IX*, Topics in Applied Physics Vol. 108, 1st ed., edited by M. Cardona and R. Merlin (Springer, Berlin, 2006), pp. 317–370.

[61] A. Bosak and M. Krisch, Inelastic x-ray scattering from phonons, in *X-Ray Diffraction*, 1st ed., edited by O. H. Seeck and B. Murphy (Pan Stanford, Singapore, 2015), Chap. 6, pp. 145–174.

[62] Beamline ID28, FIT28, version 0.6.8, ESRF — The European Synchrotron, 2021, https://www.esrf.fr/UsersAndScience/Experiments/DynExtrCond/ID28/UserManual.

[63] Rigaku Oxford Diffraction, CrysAlisPRO software system, version 1.171.38.41, Rigaku, Wrocław, Poland, 2015.

[64] J. Cosier and A. M. Glazer, A nitrogen-gas-stream cryostat for general X-ray diffraction studies, J. Appl. Crystallogr. **19**, 105 (1986).

[65] Rigaku Oxford Diffraction, CrysAlisPRO software system, version 1.171.42.54A, Rigaku, Wrocław, Poland, 2022.

[66] Bruker, SAINT, version 8.34A, Bruker AXS, Madison, WI, 2013.

[67] A. J. M. Duisenberg, Indexing in single-crystal diffractometry with an obstinate list of reflections, J. Appl. Crystallogr. **25**, 92 (1992).

[68] A. J. M. Duisenberg, L. M. J. Kroon-Batenburg, and A. M. M. Schreurs, An intensity evaluation method: *EVAL*-14, J. Appl. Crystallogr. **36**, 220 (2003).

[69] A. J. M. Duisenberg, L. M. J. Kroon-Batenburg, and A. M. M. Schreurs, EVAL Program Suite, version 20191107, University of Utrecht, Utrecht, The Netherlands, 2019.

[70] Bruker, *SADABS, version 2014/2*, Bruker AXS, Madison, WI, 2014.

[71] L. Krause, R. Herbst-Irmer, G. M. Sheldrick, and D. Stalke, Comparison of silver and molybdenum microfocus X-ray sources for single-crystal structure determination, J. Appl. Crystallogr. **48**, 3 (2015).

[72] Bruker, *TWINABS, version 2012/1*, Bruker AXS, Madison, WI, 2012.

[73] V. Petříček, M. Dušek, and L. Palatinus, Crystallographic computing system JANA2006: General features, Z. Kristallogr. - Cryst. Mater. **229**, 345 (2014).

[74] V. Petříček, M. Dušek, and L. Palatinus, Jana2006, version 23/05/2022, Department of Structure Analysis, Institute of Physics, Academy of Sciences, Prague, 2022.

[75] P. Blaha, K. Schwarz, F. Tran, R. Laskowski, G. K. H. Madsen, and L. D. Marks, WIEN2k: An APW+lo program for calculating the properties of solids, J. Chem. Phys. **152**, 074101 (2020).

[76] P. Blaha, K. Schwarz, G. Madsen, D. Kvasnicka, and J. Luitz, WIEN2k: An Augmented Plane Wave + Local Orbitals Program for Calculating Crystal Properties (Technische Universität Wien, Vienna, 2018).

[77] J. P. Perdew, K. Burke, and M. Ernzerhof, Generalized Gradient Approximation Made Simple [Phys. Rev. Lett. 77, 3865 (1996)], Phys. Rev. Lett. **78**, 1396 (1997).

[78] J. P. Perdew, K. Burke, and M. Ernzerhof, Generalized Gradient Approximation Made Simple, Phys. Rev. Lett. **77**, 3865 (1996).

[79] J. C. Toledano, Symmetry-determined phenomena at crystalline phase transitions, J. Solid State Chem. **27**, 41 (1979).

[80] H. T. Stokes and D. M. Hatch, *Isotropy Subgroups of the 230 Crystallographic Space Groups* (World Scientific, London, 1989).

[81] J.-C. Tolédano, V. Janovec, V. Kopský, J. F. Scott, and P. Boček, *Structural phase transitions*, in *Physical Properties of Crystals*, International Tables for Crystallography Vol. D, 1st ed. (International Union of Crystallography, Chester, UK, 2006), Chap. 3.1, pp. 338–376.

[82] T. Hahn and H. Klapper, *Twinning of crystals*, in *Physical Properties of Crystals*, International Tables for Crystallography Vol. D, 1st ed. (International Union of Crystallography, Chester, UK, 2006), Chap. 3.3, pp. 393–448.

[83] U. Müller, *Symmetry Relationships between Crystal Structures*, IUCr Texts on Crystallography Vol. 18 (International Union of Crystallography, Oxford, 2013), Chap. 15, pp. 197–215.

[84] The irreducible representation (irrep) T_1^+ associated with the symmetry reduction from space group *Immm* to space group $C2/m$ qualifies for a continuous transition according to Landau theory (i.e., it fulfills the Landau-Lifshitz criterion) and renormalization-group methods (see Ref. [80]).

[85] Notably, a sudden and transient increase in $I_{XRD}(T)$ at 146 K [data point marked by a star in Fig. 3(b)] may be attributed to a slight intensity instability of the primary x-ray beam.

[86] Inelastic x-ray scattering and diffuse scattering experiments at beamline ID28 of the ESRF have been performed using the same single crystal. The observed temperature shift of 9 K between the data sets may therefore be related to a minor thermal hysteresis in the structural phase transition as well as differences in the calibration of the employed open-flow N_2 coolers.

[87] Minor diffuse scattering intensity can be detected between the superstructure reflection positions at *W* even below 150 K. This residual intensity amounts to ∼0.07% of the superstructure reflection intensity at 80 K and might be linked to a subtle remaining disorder between the atomic displacements in the a_{HT}-b_{HT} plane along the c_{HT} axis.

[88] Additional IXS data in Fig. S20 of the Supplemental Material [59] demonstrate that the soft phonon branch is really a line, i.e., that the phonon energy rises sharply on moving away from the W−T path along a_{HT}^* or b_{HT}^*.

[89] M. Sato, H. Fujishita, and S. Hosnino, Neutron scattering study on the structural transition of quasi-one-dimensional conductor $K_{0.3}MoO_3$, J. Phys. C: Solid State Phys. **16**, L877 (1983).

[90] M. Hoesch, A. Bosak, D. Chernyshov, H. Berger, and M. Krisch, Giant Kohn Anomaly and the Phase Transition in Charge Density Wave $ZrTe_3$, Phys. Rev. Lett. **102**, 086402 (2009).

[91] We note that the occurrence of two modulation wave vectors $\mathbf{q} = [0.5 + \delta, 0.5 + \epsilon, 0]$ and $\mathbf{q}' = [0.5 + \delta, -(0.5 + \epsilon), 0]$ is due to pseudomerohedric twinning accompanying the reduction of space group symmetry from *Immm* (No. 71 [58]) to $C2/m$ (No. 12 [58]) in the HT-LT transition of Sc_3CoC_4 (see Refs. [46,49]).

[92] J. P. Pouget, S. M. Shapiro, G. Shirane, A. F. Garito, and A. J. Heeger, Elastic- and inelastic-neutron-scattering study of tetrathiafulvalenium-tetracyanoquinodimethanide (TTF-TCNQ): New results, Phys. Rev. B **19**, 1792 (1979).

[93] C. B. Scruby, P. M. Williams, and G. S. Parry, The role of charge density waves in structural transformations of 1*T*TaS₂, Philos. Mag. **31**, 255 (1975).

[94] O. Sezerman, A. M. Simpson, and M. H. Jericho, Thermal expansion of 1*T*-TaS₂ and 2*H*-NbSe₂, Solid State Commun. **36**, 737 (1980).

[95] D. E. Moncton, J. D. Axe, and F. J. DiSalvo, Study of Superlattice Formation in 2*H*-NbSe₂ and 2*H*-TaSe₂ by Neutron Scattering, Phys. Rev. Lett. **34**, 734 (1975).

[96] D. E. Moncton, J. D. Axe, and F. J. DiSalvo, Neutron scattering study of the charge-density wave transitions in 2*H*-TaSe₂ and 2*H*-NbSe₂, Phys. Rev. B **16**, 801 (1977).

[97] Y. Ono, Peierls transition in non-half-filled tight-binding model. I. Phase diagram, J. Phys. Soc. Jpn. **41**, 817 (1976).

[98] J. C. Tolédano and P. Tolédano, *The Landau Theory of Phase Transitions*, World Scientific Lecture Notes in Physics Vol. 3, 1st ed. (World Scientific, Singapore, 1987), Chap. V, pp. 215–306.

[99] K. N. Trueblood, H.-B. Bürgi, H. Burzlaff, J. D. Dunitz, C. M. Gramaccioli, H. H. Schulz, U. Shmueli, and S. C. Abrahams, Atomic dispacement parameter nomenclature: Report of a Subcommittee on Atomic Displacement Parameter Nomenclature, Acta Crystallogr. A: Found. Crystallogr. **52**, 770 (1996).

[100] A. Ø. Madsen, B. Civalleri, M. Ferrabone, F. Pascale, and A. Erba, Anisotropic displacement parameters for molecular crystals from periodic Hartree–Fock and density functional theory calculations, Acta Crystallogr. A: Found. Crystallogr. **69**, 309 (2013).

[101] To avoid artifacts due to parameter correlations, only XRD data collected at temperatures $T \leqslant 180$ K were fitted em-

ploying structural models in space group $C2/m$ (No. 12 [58]), while structural models in space group *Immm* (No. 71 [58]) were used for XRD data collected at higher temperatures $T > 180$ K.

[102] It should be emphasized that the unit cell doubling in the HT-LT transition of Sc_3CoC_4 cannot be recognized from the chosen cell parameter representation using an orthorhombic reference frame. This is only possible by inspection of the cell parameters within a monoclinic reference frame as given in Fig. S25 of the Supplemental Material [59].

[103] T. Janssen, G. Chapuis, and M. de Boissieu, *Aperiodic Crystals*, IUCr Monographs on Crystallography Vol. 28, 2nd ed. (International Union of Crystallography, Oxford, 2018), Chap. 6, pp. 405–443.

[104] L. R. Testardi, Structural instability and superconductivity in A-15 compounds, Rev. Mod. Phys. **47**, 637 (1975).

[105] G. R. Stewart, Superconductivity in the A15 structure, Phys. C (Amsterdam) **514**, 28 (2015).

[106] K. R. Keller and J. J. Hanak, Lattice softening in single crystal Nb_3Sn, Phys. Lett. **21**, 263 (1966).

[107] K. Carneiro, G. Shirane, S. A. Werner, and S. Kaiser, Lattice dynamics of $K_2Pt(CN)_4Br_{0.3} \cdot 3.2$ D_2O (KCP) studied by inelastic neutron scattering, Phys. Rev. B **13**, 4258 (1976).

[108] P. A. Fleury, The effects of soft modes on the structure and properties of materials, Annu. Rev. Mater. Sci. **6**, 157 (1976).

[109] G. Shirane and J. D. Axe, Phonon softening of Nb_3Sn in $[\zeta\zeta]T$ modes, Phys. Rev. B **18**, 3742 (1978).

[110] P. B. Allen, Phonons and the superconducting transition temperature, in *Metals, Superconductors, Magnetic Materials, Liquids*, Dynamical Properties of Solids Vol. 3, edited by G. K. Horton and A. A. Maradudin (North-Holland, Amsterdam, 1980), Chap. 2, pp. 95–196.

[111] J. P. Pouget, B. Hennion, C. Escribe-Filippini, and M. Sato, Neutron-scattering investigations of the Kohn anomaly and of the phase and amplitude charge-density-wave excitations of the blue bronze $K_{0.3}MoO_3$, Phys. Rev. B **43**, 8421 (1991).

[112] J. E. Lorenzo, R. Currat, P. Monceau, B. Hennion, H. Berger, and F. Levy, A neutron scattering study of the quasi-one-dimensional conductor $(TaSe_4)_2I$, J. Phys.: Condens. Matter **10**, 5039 (1998).

[113] B. Sadigh and V. Ozoliņš, Structural instability and electronic excitations in Nb_3Sn, Phys. Rev. B **57**, 2793 (1998).

[114] A. Sauer, D. A. Zocco, A. H. Said, R. Heid, A. Böhmer, and F. Weber, Electron-phonon coupling and superconductivity-induced distortion of the phonon lineshape in V_3Si, Phys. Rev. B **99**, 134511 (2019).

[115] G. Shirane and J. D. Axe, Neutron scattering study of the lattice-dynamical phase transition in Nb_3Sn, Phys. Rev. B **4**, 2957 (1971).

[116] C. W. Chu and L. R. Testardi, Direct Observation of Enhanced Lattice Stability in V_3Si under Hydrostatic Pressure, Phys. Rev. Lett. **32**, 766 (1974).

[117] R. Hoard, R. Scanlan, G. Smith, and C. Farrell, The effect of strain on the martensitic phase transition in superconducting Nb_3Sn, IEEE Trans. Magn. **17**, 364 (1981).

[118] G. F. Hardy and J. K. Hulm, The superconductivity of some transition metal compounds, Phys. Rev. **93**, 1004 (1954).

[119] B. T. Matthias, T. H. Geballe, S. Geller, and E. Corenzwit, Superconductivity of Nb_3Sn, Phys. Rev. **95**, 1435 (1954).

[120] H. J. Wallbaum, Über das Vanadiumsilizid V_3Si, Int. J. Mater. Res. **31**, 362 (1939).

[121] S. Geller, B. T. Matthias, and R. Goldstein, Some new intermetallic compounds with the "β-wolfram" structure, J. Am. Chem. Soc. **77**, 1502 (1955).

[122] H. Nowotny, R. Machenschalk, R. Kieffer, and F. Benesovsky, Untersuchungen an Silizidsystemen, Monatsh. Chem. **85**, 241 (1954).

[123] B. W. Batterman and C. S. Barrett, Crystal Structure of Superconducting V_3Si, Phys. Rev. Lett. **13**, 390 (1964).

[124] H. W. King, F. H. Cocks, and J. T. A. Pollock, Further evidence of the low temperature phase transformation in Nb_3Sn and V_3Si, Phys. Lett. A **26**, 77 (1967).

[125] R. Mailfert, B. Batterman, and J. J. Hanak, Low temperature structural transformation in Nb_3Sn, Phys. Lett. A **24**, 315 (1967).

[126] J. Wanagel and B. W. Batterman, Crystallographic study of the low-temperature phase transformation in V_3Si and Nb_3Sn, J. Appl. Phys. (Melville, NY) **41**, 3610 (1970).

[127] P. J. Brown, K.-U. Neumann, and K. R. A. Ziebeck, A polarized neutron investigation of the martensitic phase transition in V_3Si: Evidence for a band Jahn-Teller mechanism, J. Phys.: Condens. Matter **13**, 1111 (2001).

[128] P. W. Anderson and E. I. Blount, Symmetry Considerations on Martensitic Transformations: "Ferroelectric" Metals? Phys. Rev. Lett. **14**, 217 (1965).

[129] H. R. Ott, B. S. Chandrasekhar, and B. Seeber, Thermal expansion and the cubic-to-tetragonal transformation in V_3Si, Phys. Rev. B **31**, 2700 (1985).

[130] J. A. Krumhansl and Y. Yamada, Some new aspects of first-order displacive phase transformations: Martensites, Mater. Sci. Eng.: A **127**, 167 (1990).

[131] M. Acosta-Alejandro, J. Lezama-Pacheco, R. Falconi, R. Escudero, and J. Mustre de León, Local structure instability across the martensitic transition in Nb_3Sn, J. Supercond. Novel Magn. **24**, 1219 (2011).

[132] H. K. D. H. Bhadeshia, *Geometry of Crystals, Polycrystals, and Phase Transformations*, 1st ed. (CRC, Boca Raton, FL, 2018), Chap. 12, pp. 203–230.

[133] K. Hirota, L. Rebelsky, and G. Shirane, X-ray-scattering study of the cubic-to-tetragonal transition and its precursive phenomenon in V_3Si, Phys. Rev. B **51**, 11325 (1995).

[134] J. Labbé and J. Friedel, Instabilité électronique et changement de phase cristalline des composés du type V_3Si à basse température, J. Phys. France **27**, 153 (1966).

[135] S. Girault, A. H. Moudden, and J. P. Pouget, Critical x-ray scattering at the Peierls transition of the blue bronze, Phys. Rev. B **39**, 4430 (1989).

[136] H. Requardt, J. E. Lorenzo, P. Monceau, R. Currat, and M. Krisch, Dynamics in the charge-density-wave system $NbSe_3$ using inelastic x-ray scattering with meV energy resolution, Phys. Rev. B **66**, 214303 (2002).